

Hierarchical CoNi-Sulfide Nanosheet Arrays Derived from Layered Double Hydroxides toward Efficient Hydrazine Electrooxidation

Lei Zhou, Mingfei Shao,* Cong Zhang, Jingwen Zhao, Shan He, Deming Rao, Min Wei,* David G. Evans, and Xue Duan

Transition metal chalcogenides (TMCs) have recently received tremendous attention in electrochemical energy storage/conversion systems (e.g., supercapacitors,^[1–5] lithium batteries,^[6,7] and water splitting^[8–12]) due to their low cost, high stability, and electrical conductivity. Currently, preparatory protocols for TMCs materials involve high-temperature gas phase chemical vapor deposition^[13–16] and solvothermal synthesis.^[17–21] The former method is normally used for the synthesis of chalcogenide crystals, but suffers from poor reproducibility and mass production. In contrast, the solvothermal synthesis is proven with advantages of easy manipulation and facile scale-up; however, the resulting products lack tunability and are prone to aggregate in practical applications.^[22,23] Therefore, the development of green and facile synthetic routes of TMCs with well-organized structure, composition, and morphology, so as to achieve excellent electrochemical performance, is highly desirable and remains a challenge.

Layered double hydroxides (LDHs), expressed by the formula $[M^{II}_{1-x}M^{III}_x(OH)_2(A^n)_{x/n} \cdot mH_2O]$, are a typical 2D material where the tunable M^{II} and M^{III} cations are located in the brucite-like layers with a uniform and highly ordered state.^[24] By virtue of their versatility in chemical composition and architectural structure, LDH materials have been widely explored in catalysis,^[25] adsorption,^[26] and the energy field.^[27–29] In particular, a topotactic transformation process of LDH materials to self-supported metal nanoparticles would occur upon calcination in a reductive atmosphere, with unique properties of high dispersion and satisfactory stability.^[30] Stimulated by the structural merits of LDH materials, we explored a new strategy for the synthesis of supported TMCs: by using the well-defined metal nanoparticles derived from LDHs as “seeds,” a facile vulcanization reaction will occur via introducing a sulfur-containing precursor so as to obtain kinetically favored

TMCs phase. The resulting supported TMCs would inherit the intrinsic architecture and stability of the parent metal nanoparticle network, and the structure and composition can be tuned through modulating the LDH precursor and transformation conditions.

As a typical presentation, we demonstrate the fabrication of hierarchical CoNi-sulfides nanoarrays via in situ reduction of CoNi-LDH nanosheets followed by a subsequent vulcanization process, which serve as a promising catalyst in the electrooxidation of hydrazine. A synergistic effect is demonstrated in this unique structure: the conductive CoNi alloy as core provides the highway for electron transfer, and the CoNi-sulfide shell offers highly exposed active sites for electrooxidation of hydrazine. In addition, the hierarchical structure shows kinetic merits by facilitating the mass diffusion in the hydrazine oxidation. As a result, the CoNi-sulfide nanoarray exhibits excellent electrocatalytic performance in electrocatalytic hydrazine decomposition with a peak oxidation current of 9.64 mA cm^{-2} (0.8 V vs Reversible Hydrogen Electrode (RHE)), much larger than that of CoNi-oxide (5.06 mA cm^{-2}). Density functional theory (DFT) calculations reveal that the activation energy of hydrogen dissociation decreases significantly on the surface of the CoNi-sulfide shell, accounting for the largely enhanced catalytic performance. In addition, the CoNi-sulfide arrays show satisfactory long-term durability and cycling stability for hydrazine electrooxidation. This work provides a new strategy for the preparation of hierarchical TMC materials via structural transformation of LDHs precursor, which can serve as highly efficient noble metal-free anode catalysts in direct hydrazine fuel cells (DHFCs).

The fabrication process for the CoNi-alloy@CoNi-sulfide core-shell nanoarrays involves three steps, as displayed in Figure 1a. First, vertically aligned CoNi-LDH nanosheet arrays on a Ni foil substrate were prepared via a facile hydrothermal method. Subsequently, the as-obtained CoNi-LDH arrays were reduced in a hydrogen atmosphere to produce interconnected CoNi-alloy particles (denoted as CoNi-R), which serve as a conductive backbone. Afterward, a uniform layer of CoNi-sulfide was grown in situ onto the surface of as-prepared CoNi-R by a facile vulcanization process (denoted as CoNi-R-S). Figure 1b illustrates the X-ray diffraction (XRD) patterns of CoNi-LDH, CoNi-R, and CoNi-R-S, respectively. CoNi-LDH can be indexed to a rhombohedral LDH phase with an interlayer distance (d_{003}) of 0.77 nm , in accordance with the carbonate-containing LDH.^[31] The XRD pattern of the CoNi-R material shows (111) and (200) reflection of the cubic CoNi alloy phase.^[32,33]

L. Zhou, Dr. M. F. Shao, C. Zhang, Dr. S. He,
D. M. Rao, Prof. M. Wei, Prof. D. G. Evans, Prof. X. Duan
State Key Laboratory of Chemical Resource Engineering
Beijing University of Chemical Technology
Beijing 100029, China
E-mail: shaomf@mail.buct.edu.cn;
weimin@mail.buct.edu.cn
Dr. J. W. Zhao
Qingdao Industrial Energy Storage Research Institute
Qingdao Institute of Bioenergy and Bioprocess Technology
Chinese Academy of Science
Qingdao 266101, China



DOI: 10.1002/adma.201604080

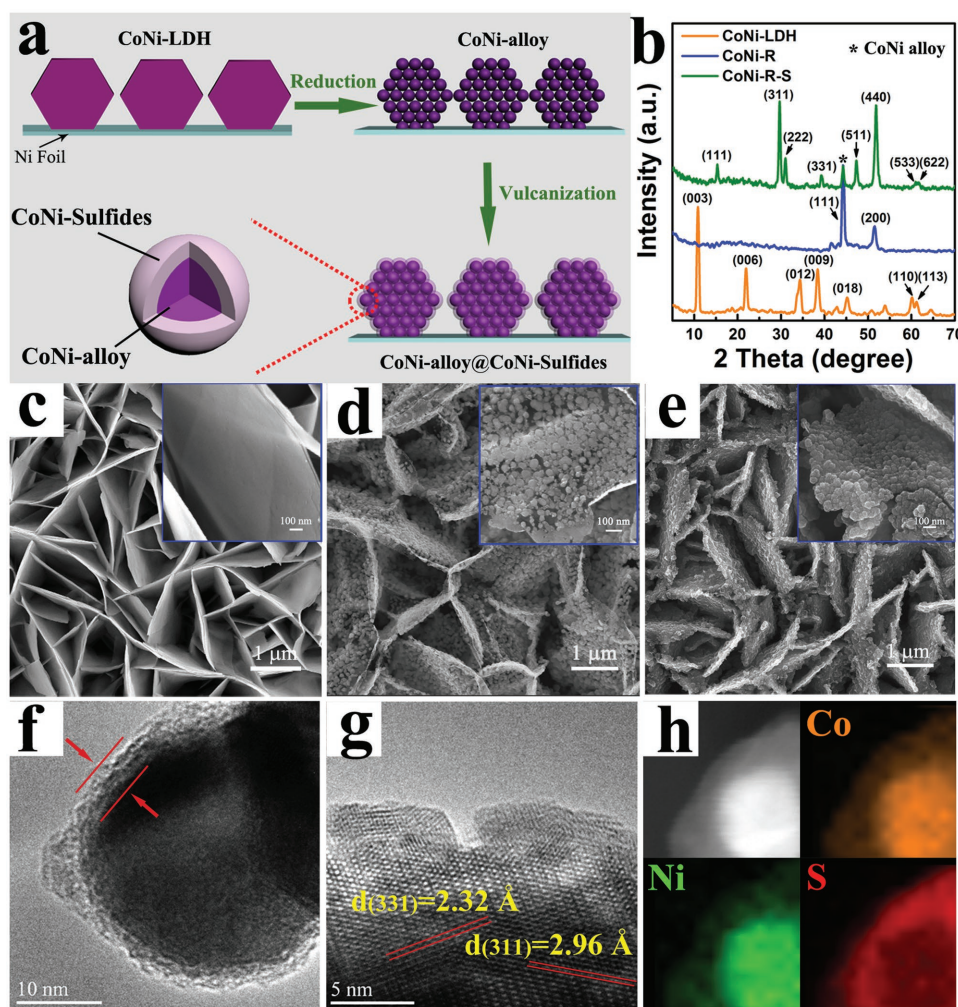


Figure 1. a) Schematic illustration for the synthesis of CoNi-alloy@CoNi-sulfide nanoarrays. b) XRD patterns of CoNi-LDH, CoNi-R, and CoNi-R-S (all the samples are scraped from the substrate for measurement). SEM images for c) CoNi-LDH, d) CoNi-R, and e) CoNi-R-S, respectively. f) TEM image, g) crystal fringes, and h) HAADF-STEM image and EDX mapping of CoNi-R-S.

In the case of the CoNi-R-S sample, the superimposition of a CoNi alloy phase and a $(\text{Co,Ni})_9\text{S}_8$ phase (JCPDS No. 12-0723) is observed. No other crystalline phase is detected, implying the high purity of the final CoNi-alloy@CoNi-sulfide with core-shell nanostructure.

The scanning electron microscopy (SEM) image of CoNi-LDH nanoarrays displays an intercrossed nanowall network in which the LDH microcrystals (with a lateral size of $\approx 2 \mu\text{m}$) stand perpendicularly on the substrate (Figure 1c). The reduction of CoNi-LDH nanoarrays does not deteriorate their ordered array structure (Figure 1d); one single nanosheet of CoNi-R is composed of connected CoNi alloy nanoparticles with an average size of $\approx 44 \text{ nm}$ (Figure 1d, inset). After the vulcanization process, the resulting CoNi-R-S maintains the original nanosheet morphology, with an enhanced thickness from ≈ 40 to $\approx 50 \text{ nm}$ (Figure 1e). The transmission electron microscopy (TEM) image of a CoNi-R-S nanoparticle displays a clear boundary between the CoNi-alloy core (diameter: $\approx 32 \text{ nm}$) and the CoNi-sulfide shell (thickness: $\approx 7 \text{ nm}$) (Figure 1f). The

high-resolution transmission electron microscopy (HR-TEM) image reveals interplanar distance of 0.23 and 0.29 nm that can be attributed to the (311) and (311) plane of the CoNi-sulfide phase, respectively (Figure 1g). The typical high-angle annular dark-field scanning TEM (HAADF-STEM) image of an individual CoNi-R-S nanoparticle and corresponding energy-dispersive X-ray spectrometry (EDS) mapping verify the well-defined CoNi-alloy core/CoNi-sulfide shell structure (Figure 1h): the elements Co and Ni show a high density in the core while S is located in the shell. The EDS line scanning (Figure S1, Supporting Information) further confirms this architecture, in which the Co/Ni molar ratio is ≈ 1.9 . For comparison, the CoNi-alloy@CoNi-oxide (denoted CoNi-R-O) was prepared as a reference sample (see the Supporting Information for detailed preparation), with a similar hierarchical morphology and core-shell structure (Figure S2, Supporting Information). In addition, the transformation of CoNi alloy to CoNi-alloy@CoNi-sulfide arrays with different sulfuration time is also studied (Figure S3, Supporting Information). As shown in

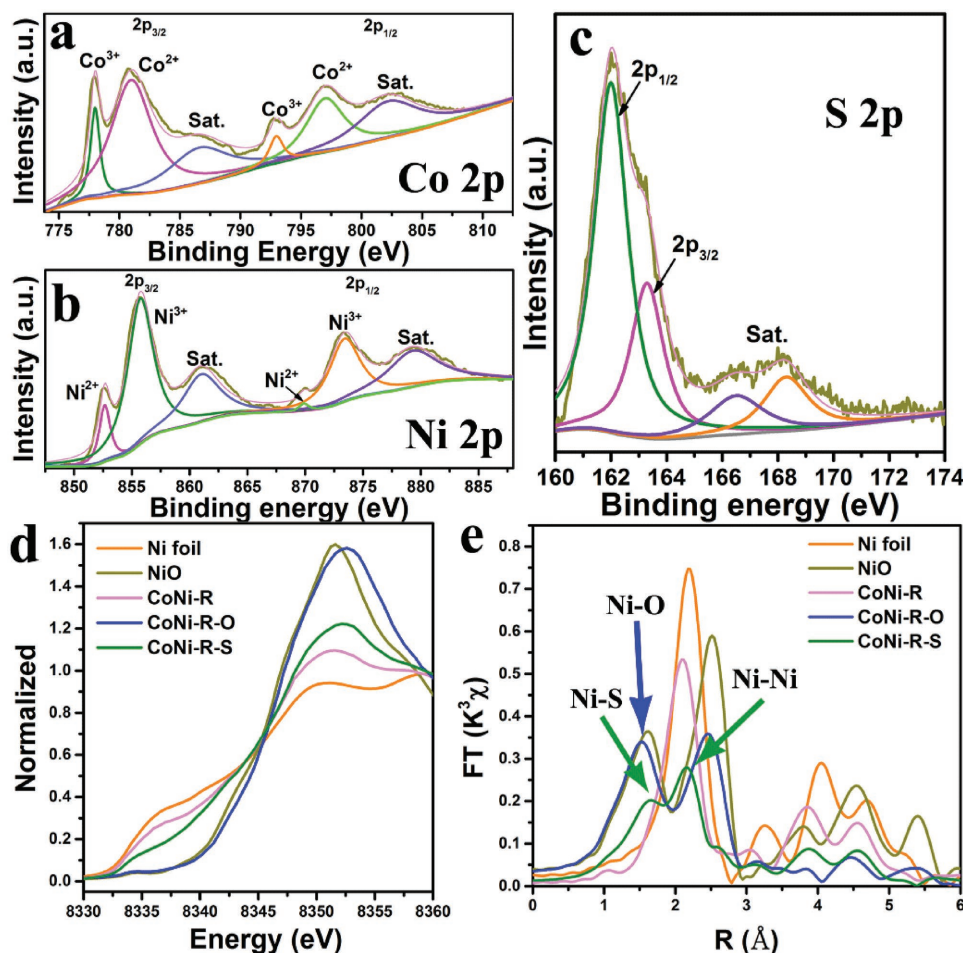


Figure 2. a) Co 2p, b) Ni 2p, and c) S 2p orbital XPS spectra for the sample of CoNi-R-S. d) Normalized intensity of Ni K-edge XANES spectra and e) the corresponding Fourier transforms of CoNi-R, CoNi-R-O, and CoNi-R-S with Ni foil and NiO as references.

Figure S3a (Supporting Information), the nanosheet consisting of interconnected nanoparticles gradually becomes dominant with the epitaxial growth of CoNi-sulfide shell on the surface of the CoNi alloy framework along with the sulfurization. Some unoccupied interspace is clearly observed in the early sulfurization stage (before 0.5 h, Figure S3b, Supporting Information), but gets smaller along with the increase of the thickness of CoNi-sulfide layer (1.5 h, Figure S3c, Supporting Information). As the sulfurization time reaches 3 h (Figure S3d, Supporting Information), a dense packing of CoNi-alloy@CoNi-sulfide nanoparticles in the nanosheets is obtained.

X-ray photoelectron spectroscopy (XPS) was conducted to further investigate the chemical composition of the CoNi-R-S sample. The survey spectrum of CoNi-R-S indicates the presence of Co, Ni, and S (Figure S4, Supporting Information). **Figure 2a–c** shows the Co 2p, Ni 2p, and S 2p core-level spectra of the as-synthesized CoNi-R-S arrays, respectively. The Co 2p_{3/2} spectrum displays a complex situation broadened by the multiplet splitting effect (Figure 2a), whose binding energy can be deconvoluted to 780.1 eV (Co²⁺) and 781.6 eV (Co³⁺), respectively.^[34] However, it is hard to confirm the existence of Co⁰ due to the rather close binding energies of Co⁰ and Co³⁺.^[35] The

binding energy of Ni 2p_{3/2} can be fitted with two spin-orbit doublets (Figure 2b), characteristic of Ni²⁺ and Ni³⁺.^[36] In the case of S 2p (Figure 2c), the peak at 162.1 eV is attributed to S²⁻.^[37] The chemical composition of CoNi-R-S containing Co³⁺, Co²⁺, Ni²⁺, Ni³⁺, and S²⁻ agrees well with the results of (Co,Ni)₉S₈. In addition, the powdered sample of CoNi-R-S shows magnetic property, which can be rapidly separated by a magnet within a few seconds (Figure S5, Supporting Information). It is reported that the superficial oxidation of CoNi alloy or CoNi-sulfide is unavoidable when exposed in air.^[37,38] A slight oxidation of CoNi-R and CoNi-R-S occurs during the preparation and storage of catalysts. However, the XPS elemental analysis of the CoNi-R-S electrode stored under ambient condition for 1 week and 2 weeks (Figure S6 and Table S1, Supporting Information) shows that the oxygen content can be maintained at a relatively low degree even after a long-time exposed in air.

X-ray absorption near-edge structure (XANES) spectroscopy was performed to provide electronic structure information, and Fourier transform of Ni K-edge was used to illustrate the detailed atomic configuration. The ambient temperature/atmosphere XANES spectra of CoNi-R-S, CoNi-R-O, and CoNi alloy (Ni and NiO as references) are displayed in Figure 2d.

The white line of CoNi-R-O almost coincides with NiO reference, indicating NiO is the dominated phase in this oxide. The white line intensity of CoNi-R-S is significantly lower than that of NiO but higher than Ni foil, indicating the existence of Ni^{δ+} ($0 < \delta < 2$) species in CoNi-R-S sample.^[39] Furthermore, the pre-edge feature can give more information about Ni coordination and symmetry. The CoNi-R-S shows distinct changes in the pre-edge features compared with Ni foil, which is probably attributed to the heteroatomic interaction and the variations in the Ni coordination structure (e.g., the formation of Ni–S and Ni–Co coordination). A similar situation is also observed in the pre-edge features of Co K-edge spectra (Figure S7a, Supporting Information). The Fourier transform of Ni K-edge extended X-ray adsorption fine structure (EXAFS) oscillations was further used to study the detailed atomic configuration for CoNi-R-S (Figure 2e). In the R-space spectrum of CoNi-R-S, the peak centered at ≈ 0.240 nm is attributed to Ni–Ni coordination; a new bond (Ni–S coordination centered at ≈ 0.160 nm) appears compared with pristine CoNi alloy, in accordance with the results of XRD (Figure 1b). The peak intensity of Ni–Ni bond in CoNi-R-S decreases significantly accompanying a peak shift to a high R value, which demonstrates a largely reduced Ni–Ni bonding resulting from the incorporation of the S element. Figure S7b (Supporting Information) displays two peaks centered at ≈ 0.199 and 0.218 nm attributed to Co–S and Co–Co coordination in CoNi-R-S. The results above demonstrate the

successful incorporation of S into CoNi alloy, resulting in the coexistence of the CoNi alloy core and CoNi-sulfide shell.

The electrochemical performance of CoNi-R-S and corresponding reference samples toward hydrazine electrooxidation were subsequently evaluated in an alkaline medium (0.1 M KOH). The potential window for HzOR oxidation is limited from -0.1 to 1.0 V (vs RHE) according to the liner sweep voltammograms (LSV) in 0.1 M KOH (Figure S8, Supporting Information) to avoid the side reaction. Figure 3a shows the cyclic voltammograms (CVs) of the five samples recorded in 0.1 M KOH solution without hydrazine (blue lines). A pair of redox peaks is observed for the samples of CoNi-R, CoNi-R-O, and CoNi-R-S, corresponding to the reversible redox of Ni³⁺/Ni²⁺ and Co³⁺/Co²⁺ associated with OH⁻. In the presence of 20×10^{-3} M hydrazine (Figure 3a, pink lines), the CoNi-R-S electrode displays the lowest onset potential and the highest current density from -0.1 to 1.0 V (vs RHE) among CoNi-LDH, CoNi-R, CoNi-R-O, and CoNi-R-S, indicating the highest electrochemical activity. LSV results of the five electrodes are shown in Figure S9 (Supporting Information). At the same potential of 0.8 V (vs RHE), the as-prepared CoNi-R-S affords a current density of 9.64 mA cm⁻², which is 2.0 times, 2.1 times, 2.4 times, and 5.1 times higher than that of CoNi-R-O, CoNi-LDH, CoNi-R, and Ni foil substrate, respectively. The current densities at 0.8 V (vs RHE) in a series of hydrazine concentrations are shown in Figure 3b. With the increase of hydrazine

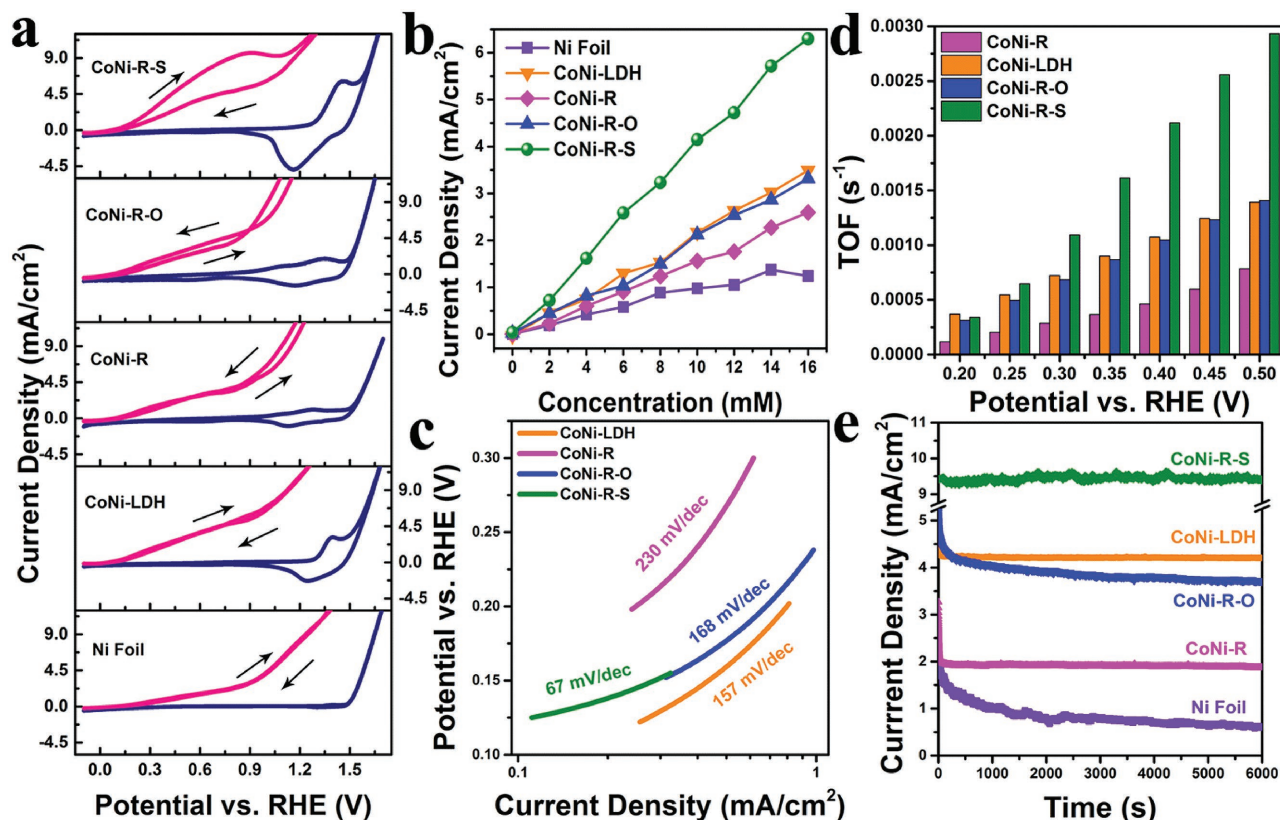


Figure 3. a) CV curves of hydrazine electrooxidation over Ni foil, CoNi-LDH, CoNi-R, CoNi-R-O, and CoNi-R-S, in 0.1 M KOH (blue lines) and 0.1 M KOH + 20×10^{-3} M hydrazine (pink lines). b) Current densities at each peak potential obtained from the CVs as a function of hydrazine concentration. c) Tafel plots, d) TOF values, and e) stability test of CoNi-R-S and various control samples.

concentration, a positive correlation between peak current and hydrazine concentration is observed. In order to further study the electrooxidation of hydrazine with a high concentration, LSV curves of Ni foil, CoNi-LDH, CoNi-R, CoNi-R-O, and CoNi-R-S in 2 M hydrazine are displayed in Figure S10 (Supporting Information). It is found that the oxidation current density enhances gradually with the increase of hydrazine concentration for all these catalysts; and the CoNi-R-S exhibits the highest current density in the whole concentration range (from 9.04 mA cm⁻² to 117.8 mA cm⁻² at 1.0 V vs RHE) compared with other samples (Table S2, Supporting Information).

The Tafel slope of CoNi-R-S is calculated to be 67 mV dec⁻¹ (Figure 3c), much smaller than that of CoNi-R-O (168 mV dec⁻¹), CoNi-R (230 mV dec⁻¹), and CoNi-LDH (157 mV dec⁻¹), illustrating the robust hydrazine electrooxidation kinetics over CoNi-R-S. The activity of as-obtained catalysts was further investigated in apparent turnover frequencies (TOFs) (Figure 3d; see the Supporting Information for calculation details). The CoNi-R-S possesses the largest TOF value in the whole test range especially at a high potential. For instance, CoNi-R-S, CoNi-R-O, CoNi-R, and CoNi-LDH give TOF values of 0.00293 s⁻¹, 0.00141 s⁻¹, 0.00139 s⁻¹, and 0.00078 s⁻¹ at 0.8 V (vs RHE), respectively. This confirms that the existence of CoNi-sulfide significantly promotes the rate of hydrazine decomposition compared with CoNi-oxide and CoNi-LDH, consistent with the results of the Tafel slope. Moreover, the faradaic efficiencies of hydrazine electrooxidation (0.1 M KOH, 20 × 10⁻³ M hydrazine) at 0.5 V and 1.0 V versus RHE are 99.2% and 99.8%, respectively, indicating a high level of electron utilization (Figure S11, Supporting Information). In addition, the residual hydrazine content in electrolyte after the electrooxidation test was measured by UV-vis absorption spectrum^[40] (Figure S12a,b, Supporting Information), which is in accordance with the theoretical results (Table S3, Supporting Information). This demonstrates that the hydrazine oxidation is the dominant reaction during the electrocatalytic process. The effect of the Co:Ni ratio of CoNi-sulfides on their electrocatalytic performance has been investigated; and two reference samples, CoNi₂-sulfide and Co₄Ni-sulfide, were prepared based on the same method. XRD spectra and SEM images show the same crystal structure with CoNi-sulfide and a rather similar morphology (Figure S13a–c, Supporting Information). XPS results (Figure S13d and Table S4, Supporting Information) give a Co:Ni ratio of approximately 1:2 and 4:1 for CoNi₂-sulfide and Co₄Ni-sulfide, respectively. LSV results (Figure S13e, Supporting Information) show that the sample of CoNi-R-S (Co:Ni = 2:1) exhibits the largest current density at various potentials, indicating the best catalytic behavior toward hydrazine electrooxidation.

To further evaluate the electrocatalytic activity and stability of CoNi-R-S hierarchical nanoarrays under continuous operating conditions, long-term chronoamperometric tests were carried out in a 0.1 M KOH + 20 × 10⁻³ M hydrazine solution. Figure 3e shows the current density curve versus time recorded at 0.8 V (vs RHE) for 6000 s. No obvious change in the oxidation current is observed for CoNi-R-S after 6000 s (retention: 99.6%), superior to CoNi-R-O (75.7%), CoNi-LDH (91.6%), CoNi-R (80.3%), and Ni foil (25.8%). The structure and composition of CoNi-sulfide after long-term stability test were studied by using

SEM, HR-TEM, and XRD measurements (Figure S14a,b,d, Supporting Information). The SEM image does not show obvious morphological change after 6000 s test (Figure S14a, Supporting Information), with the original core-shell structure revealed by HR-TEM (Figure S14b, Supporting Information). In contrast, the CoNi-R-O sample displays a structural collapse after catalytic cycling (Figure S14c, Supporting Information), accounting for the current decay for CoNi-R-O. XRD patterns of CoNi-R-S display the same crystal structure as the fresh catalyst (Figure S14d, Supporting Information), indicating the stable structure of CoNi-sulfide. Furthermore, the element composition of CoNi-sulfide remains unchanged according to EDS and XPS elemental analysis (Figure S14e and Tables S5 and S6, Supporting Information). Particularly, the leaching of S is negligible, accounting for the excellent electrocatalytic performance of CoNi-R-S for hydrazine oxidation. The XPS results of CoNi-oxide and CoNi-sulfide (before and after stability test) are displayed in Figure S15 (Supporting Information). The composition and state of Co and Ni in CoNi-oxide and CoNi-sulfide do not show significant change after the stability test, indicating their chemical stability in electrocatalytic oxidation of hydrazine. The obtained Nyquist plot by electrochemical impedance spectra (EIS) experiments shows negligible changes of R_s and R_{ct} (in the corresponding equivalent circuit) for CoNi-R-S after stability test (Figure S16, Supporting Information), indicating a consistent conductivity and charge-transfer kinetics. This indicates that the CoNi-R-S catalyst exhibits largely enhanced long-term durability for hydrazine electrooxidation in alkaline media. In addition, the EIS and LSV results of the CoNi-R-S electrode do not exhibit obvious variation when stored under ambient condition for 1 week and 2 weeks (Figure S17a,b, Supporting Information), demonstrating a high chemical stability. An electrolytic cell was fabricated by using the CoNi-R-S electrode as cathode and Pt wire as anode, with one 1.5 V AA battery acting as the power source (Figure S18, Supporting Information). No gas release is found without applied voltage (Figure S18a, Supporting Information), which excludes the direct reaction between CoNi-sulfide and hydrazine. In contrast, a rapid bubble release is observed as the circuit is closed (Figure S18b, Supporting Information), illustrating facile reaction kinetics of hydrazine electrooxidation in the presence of CoNi-R-S.

To reveal the relationship between the core-shell CoNi-R-S and its catalytic process, CoNi-sulfide without the CoNi alloy core (denoted as CoNi-S) was prepared by direct vulcanization of CoNi-LDH arrays (Figure S19a, Supporting Information). The EIS test was performed to gain insight into the electron transportation ability. The diameter of semicircle demonstrates the charge-transfer resistance (R_{ct} in the corresponding equivalent circuit). The R_{ct} in the Nyquist plot for CoNi-R-S is much smaller than that of CoNi-S (Figure S19b, Supporting Information), indicating a lower charge-transfer resistance of CoNi-R-S. This is further confirmed by the corresponding LSV results (Figure S19c, Supporting Information) and Tafel slope (Figure S19d, Supporting Information). Moreover, the CoNi-R-S electrode shows a much smaller R_{ct} value (1.5 Ω) than that of CoNi-R-O (4.7 Ω) (Figure S20, Supporting Information), indicating accelerated kinetics for hydrazine electrooxidation over CoNi-sulfide. In addition, the slope of the

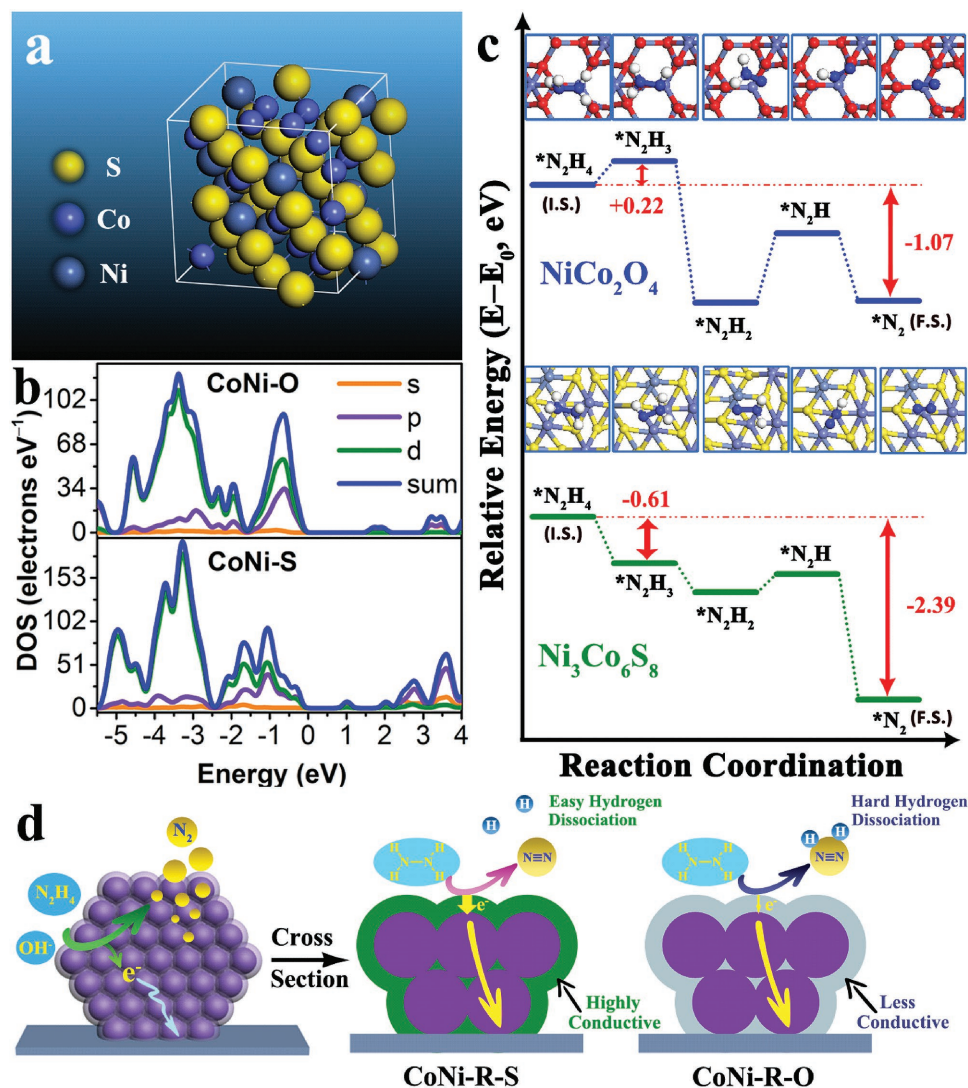


Figure 4. a) The model of $\text{Ni}_3\text{Co}_6\text{S}_8$. b) Total and partial electronic density of states (TDOS and PDOS) calculated for CoNi-sulfide and CoNi-oxide (the Fermi level is set at 0 eV). c) The energy profiles for the reaction pathways over CoNi-sulfide and CoNi-oxide. d) A schematic illustration for the hydrazine oxidation catalyzed by CoNi-R-S and CoNi-R-O.

linear part in the Nyquist plot for CoNi-R-S is larger than that of CoNi-S and CoNi-R-O, indicating the hierarchical structure of CoNi-R-S facilitates the electrolyte ionic diffusion. Therefore, the improved conductivity and mass transport in the CoNi-R-S system promote its electrocatalytic performance.

DFT calculations were carried out to give an insight into the activity of CoNi-alloy@CoNi-sulfide toward hydrazine electrooxidation. The as-obtained CoNi-sulfide ($\text{Ni}_3\text{Co}_6\text{S}_8$) possesses a face-centered cubic structure (Figure 4a).^[41] The CoNi-oxide (NiCo_2O_4) with face-centered cubic structure was used as a control sample (Figure S21, Supporting Information). Figure S22 (Supporting Information) illustrates the DOS values of each element in $\text{Ni}_3\text{Co}_6\text{S}_8$; the main contribution to DOS originates from the d orbitals of the Ni/Co atom and p orbital of the S atom, proving the Ni–S/Co–S hybridization in CoNi-sulfide. The calculated DOS values of $\text{Ni}_3\text{Co}_6\text{S}_8$ and NiCo_2O_4 exhibit the semiconductor property, in which the energy bands

are not continuous near the Fermi level (Figure 4b). However, the bandgap of $\text{Ni}_3\text{Co}_6\text{S}_8$ (0.75 eV) is much smaller than that of NiCo_2O_4 (1.45 eV), suggesting a better electron transportation ability in $\text{Ni}_3\text{Co}_6\text{S}_8$, which is consistent with the EIS results (Figure S20, Supporting Information). Previous studies reported that the decomposition of N_2H_4 relates to the elongation of the N–H bond, involving four consecutive dehydrogenation steps ($\text{N}_2\text{H}_4 \rightarrow \text{N}_2\text{H}_3 \rightarrow \text{N}_2\text{H}_2 \rightarrow \text{N}_2\text{H} \rightarrow \text{N}_2$).^[42,43] The average charge density of CoNi-sulfide and CoNi-oxide obtained from population analysis is displayed in Table S7 (Supporting Information). It is found that the charge density of the Ni species in CoNi-sulfide is much lower than that in CoNi-oxide, which would facilitate the adsorption of the N_2H_4 molecule.^[44,45] To evaluate the effect of electronic structure on the hydrazine oxidation, the intramolecular dehydrogenation of N_2H_4 on the surface of CoNi-sulfide and CoNi-oxide was calculated, respectively (Figure 4c). We investigate the stepwise

dehydrogenation process of hydrazine over the (311) surface of CoNi-sulfide and CoNi-oxide according to the HR-TEM results (Figure 1g). The optimized structures of N_2H_4 adsorbed onto the surface of sulfide or oxide are used as the initial state of hydrazine oxidation. First, the transformation from adsorbed N_2H_4 to N_2H_3 is exothermic by 0.61 eV on the surface of CoNi-sulfide but endothermic by 0.22 eV on the surface of CoNi-oxide. This indicates that the dissociation of first H atom from adsorbed N_2H_4 is more thermodynamically favorable on the CoNi-sulfide than CoNi-oxide. Similarly, the third step from adsorbed N_2H_2 to N_2H needs to overcome a higher activation energy on the surface of CoNi-oxide (0.64 eV) than CoNi-sulfide (0.23 eV). In addition, the energy difference from the adsorbed N_2H_4 (initial state) to adsorbed N_2 (final state) is exothermic by 2.39 eV on the surface of CoNi-sulfide, much larger than that on CoNi-oxide (1.07 eV), indicating a more thermodynamically favorable catalytic process over CoNi-sulfide. Therefore, the whole process is close to “going downstairs” on CoNi-sulfide instead of “climbing mountains” on CoNi-oxide, accounting for the superior electrocatalytic performance of CoNi-sulfide toward hydrazine oxidation.

Based on the discussion above, the CoNi-R-S exhibits excellent hydrazine electrooxidation performance including high current density, low Tafel slope, and large TOF value, which can be explained as shown in Figure 4d. First, the CoNi-sulfide affords a facile dehydrogenation process of the hydrazine molecule confirmed by the DFT calculation, which intrinsically determines its electrocatalytic activity. Second, both the CoNi-alloy core and CoNi-sulfide shell in CoNi-R-S are highly conductive (Figures S19b and S20, Supporting Information), which benefits the electron transportation during the reaction process. In addition, the hierarchical structure facilitates the penetration of the electrolyte and reduces the ionic diffusion path, benefiting the mass diffusion in the hydrazine oxidation.

In summary, a hierarchical nanostructure with the CoNi-sulfide shell grown on the surface of the CoNi-alloy network was synthesized by topo-transformation of CoNi-LDH arrays. The resulting CoNi-alloy@CoNi-sulfide displays excellent catalytic activity and robust durability for hydrazine electrooxidation, compared with the CoNi-alloy@CoNi-oxide, CoNi-sulfide, and CoNi-LDH. This is ascribed to the facile dehydrogenation process on the surface of CoNi-sulfide, largely enhanced electron conductivity, and ion transport in this hierarchical core-shell nanostructure. It is expected that the approach can be extended to the fabrication of other sulfides with potential applications in fuel cells and electrocatalysis.

Supporting Information

Supporting Information is available from the Wiley Online Library or from the author.

Acknowledgements

This work was supported by the National Natural Science Foundation of China (NSFC), the 973 Program (Grant No. 2014CB932102), and the Fundamental Research Funds for the Central Universities (buctrc201506;

YS 1406). M. Wei particularly appreciates the financial aid from the China National Funds for Distinguished Young Scientists of the NSFC.

Received: August 1, 2016

Revised: October 13, 2016

Published online: December 5, 2016

- [1] X. Y. Yu, L. Yu, X. W. Lou, *Adv. Energy Mater.* **2016**, *6*, 14.
- [2] L. Yu, L. Zhang, H. B. Wu, X. W. Lou, *Angew. Chem. Int. Ed.* **2014**, *53*, 3711.
- [3] X. Y. Yu, L. Yu, H. B. Wu, X. W. Lou, *Angew. Chem. Int. Ed.* **2015**, *54*, 5331.
- [4] W. J. Zhou, X. H. Cao, Z. Y. Zeng, W. H. Shi, Y. Y. Zhu, Q. Y. Yan, H. Liu, J. Y. Wang, H. Zhang, *Energy Environ. Sci.* **2013**, *6*, 2216.
- [5] R. Zou, Z. Zhang, M. F. Yuen, J. Hu, C. S. Lee, W. Zhang, *Sci. Rep.* **2015**, *5*, 7862.
- [6] A. Douglas, R. Carter, L. Oakes, K. Share, A. P. Cohn, C. L. Pint, *ACS Nano* **2015**, *9*, 11156.
- [7] Z. Hu, L. Wang, K. Zhang, J. Wang, F. Cheng, Z. Tao, J. Chen, *Angew. Chem. Int. Ed.* **2014**, *53*, 12794.
- [8] H. Zhu, J. Zhang, R. Yan Zhang, M. Du, Q. Wang, G. Gao, J. Wu, G. Wu, M. Zhang, B. Liu, J. Yao, X. Zhang, *Adv. Mater.* **2015**, *27*, 4752.
- [9] B. You, Y. Sun, *Adv. Energy Mater.* **2016**, *6*, 1502333.
- [10] H. Wang, Z. Li, G. Li, F. Peng, H. Yu, *Catal. Today* **2015**, *245*, 74.
- [11] W. Zhou, X.-J. Wu, X. Cao, X. Huang, C. Tan, J. Tian, H. Liu, J. Wang, H. Zhang, *Energy Environ. Sci.* **2013**, *6*, 2921.
- [12] L. J. Yang, W. J. Zhou, D. M. Hou, K. Zhou, G. Q. Li, Z. H. Tang, L. G. Li, S. W. Chen, *Nanoscale* **2015**, *7*, 5203.
- [13] Y. H. Lee, X. Q. Zhang, W. Zhang, M. T. Chang, C. T. Lin, K. D. Chang, Y. C. Yu, J. T. Wang, C. S. Chang, L. J. Li, T. W. Lin, *Adv. Mater.* **2012**, *24*, 2320.
- [14] I. Song, C. Park, M. Hong, J. Baik, H. J. Shin, H. C. Choi, *Angew. Chem. Int. Ed.* **2014**, *53*, 1266.
- [15] Q. Zhang, X. Xiao, R. Zhao, D. Lv, G. Xu, Z. Lu, L. Sun, S. Lin, X. Gao, J. Zhou, C. Jin, F. Ding, L. Jiao, *Angew. Chem. Int. Ed.* **2015**, *54*, 8957.
- [16] Y. Zhan, Z. Liu, S. Najmaei, P. M. Ajayan, J. Lou, *Small* **2012**, *8*, 966.
- [17] W. Bryks, M. Wette, N. Velez, S. W. Hsu, A. R. Tao, J. Am. Chem. Soc. **2014**, *136*, 6175.
- [18] A. W. Tang, S. C. Qu, K. Li, Y. B. Hou, F. Teng, J. Cao, Y. S. Wang, Z. G. Wang, *Nanotechnology* **2010**, *21*, 9.
- [19] P. L. Saldanha, R. Brescia, M. Prato, H. B. Li, M. Povia, L. Manna, V. Lesnyak, *Chem. Mater.* **2014**, *26*, 1442.
- [20] G. X. Ma, Y. L. Zhou, X. Y. Li, K. Sun, S. Q. Liu, J. Q. Hu, N. A. Kotov, *ACS Nano* **2013**, *7*, 9010.
- [21] Y. Y. Kim, D. Walsh, *Nanoscale* **2010**, *2*, 240.
- [22] A. M. Wiltrout, C. G. Read, E. M. Spencer, R. E. Schaak, *Inorg. Chem.* **2016**, *55*, 221.
- [23] W. Du, Z. Zhu, Y. Wang, J. Liu, W. Yang, X. Qian, H. Pang, *RSC Adv.* **2014**, *4*, 6998.
- [24] Q. Wang, D. O'Hare, *Chem. Rev.* **2012**, *112*, 4124.
- [25] J. T. Feng, Y. F. He, Y. N. Liu, Y. Y. Du, D. Q. Li, *Chem. Soc. Rev.* **2015**, *44*, 5291.
- [26] S. L. Ma, Y. Shim, S. M. Islam, K. S. Subrahmanyam, P. L. Wang, H. Li, S. C. Wang, X. J. Yang, M. G. Kanatzidis, *Chem. Mater.* **2014**, *26*, 5004.
- [27] M. Shao, R. Zhang, Z. Li, M. Wei, D. G. Evans, X. Duan, *Chem. Commun.* **2015**, *51*, 15880.
- [28] C. Tang, H. S. Wang, H. F. Wang, Q. Zhang, G. L. Tian, J. Q. Nie, F. Wei, *Adv. Mater.* **2015**, *27*, 4516.
- [29] T. C. Chen, Q. Zhang, M. Q. Zhao, J. Q. Huang, C. Tang, F. Wei, *Carbon* **2015**, *95*, 292.

- [30] G. L. Fan, F. Li, D. G. Evans, X. Duan, *Chem. Soc. Rev.* **2014**, *43*, 7040.
- [31] M. Shao, F. Ning, M. Wei, D. G. Evans, X. Duan, *Adv. Funct. Mater.* **2014**, *24*, 580.
- [32] J. Feng, F. Pu, Z. Li, X. Li, X. Hu, J. Bai, *Carbon* **2016**, *104*, 214.
- [33] Y. Hou, H. Yuan, Z. Wen, S. Cui, X. Guo, Z. He, J. Chen, *J. Power Sources* **2016**, *307*, 561.
- [34] L. Shen, J. Wang, G. Xu, H. Li, H. Dou, X. Zhang, *Adv. Energy Mater.* **2015**, *5*, 1400977.
- [35] C. Wang, X. Bai, S. Liu, L. Liu, *J. Mater. Sci.* **2004**, *39*, 6191.
- [36] V. H. Nguyen, C. Lamiel, J.-J. Shim, *Electrochim. Acta* **2015**, *161*, 351.
- [37] L. Wan, J. W. Xiao, F. Xiao, S. Wang, *ACS Appl. Mater. Interfaces* **2014**, *6*, 7735.
- [38] J. W. Xiao, L. Wan, S. H. Yang, F. Xiao, S. Wang, *Nano Lett.* **2014**, *14*, 831.
- [39] Y. Chen, C. Li, J. Zhou, S. Zhang, D. Rao, S. He, M. Wei, D. G. Evans, X. Duan, *ACS Catal.* **2015**, *5*, 5756.
- [40] A. D. Smolenkov, I. A. Rodin, O. A. Shpigun, *J. Anal. Chem.* **2012**, *67*, 98.
- [41] H. R. Chauke, D. Nguyen-Manh, P. E. Ngoepe, D. G. Pettifor, S. G. Fries, *Phys. Rev. B* **2002**, *66*, 115105.
- [42] P.-X. Zhang, Y.-G. Wang, Y.-Q. Huang, T. Zhang, G.-S. Wu, J. Li, *Catal. Today* **2011**, *165*, 80.
- [43] M. D. Esrafil, V. Mokhtar Teymurian, R. Nurazar, *Surf. Sci.* **2015**, *632*, 118.
- [44] Y.-J. Zhong, H.-B. Dai, Y.-Y. Jiang, D.-M. Chen, M. Zhu, L.-X. Sun, P. Wang, *J. Power Sources* **2015**, *300*, 294.
- [45] Y. Jiang, Q. Kang, J. Zhang, H.-B. Dai, P. Wang, *J. Power Sources* **2015**, *273*, 554.